Computational Mechanics
https://doi.org/10.1007/s00466-026-02825-3

ORIGINAL PAPER

A nonlinear 10-node tetrahedral element based on a Hu-Washizu variational formulation

Friedrich Gruttmann[1] · Werner Wagner[2]

Received: 14 April 2026 / Revised: 5 June 2026 / Accepted: 2 July 2026

Abstract
In this paper a new nonlinear 10–node tetrahedral element is described. A Hu–Washizu functional with independent displacements, stresses and strains is the variational basis of the finite element formulation. The shape functions of the independent quantities are specified. Elimination of the stress and strain parameters on element level leads to a mixed hybrid element. The patch test is fulfilled in the common linear and also in a nonlinear version. The element is characterized by a remarkable robustness with the possibility of very large load steps in nonlinear applications. The total number of iterations is significantly lower than that of the corresponding displacement element. This holds especially for thin structures subjected to bending deformations. The performance of the new element in comparison to existing approaches is illustrated by means of representative numerical simulations.

Keywords Hu–Washizu variational principle · 10-node tetrahedral element · Quasi incompressible material behavior · Large load steps with few iterations

1 Introduction

Nonlinear numerical analysis of structures requires effective and robust element formulations. Especially the possibility of large solution steps and high accuracy when using reasonable unstructured meshes are desired properties. In many engineering fields finite elements meshes are generated with commercial software tools. For complex three-dimensional geometries these programs prefer tetrahedral elements rather than brick elements. Additionally these elements facilitate adaptive mesh refinement. Standard linear 4-node tetrahedral and 8-node hexahedral displacement elements show rather poor performance in finite element analysis involving bending dominated problems and locking response in the nearly incompressible limit. It is well known that these difficulties can be circumvented by application of high order elements. Within the p-method locking response disappears when sufficient high order polynomials are used. Alternatively, element formulations can be derived using mixed variational principles.

Mixed low order elements, like 4-node elements in the 2D case and 8-node elements in the 3D case, have been considered in early publications, e.g. [1, 2]. The elements are mainly based on assumed stress hybrid formulations. The basis for these methods are multi-field variational principles. Especially for linear elasticity the Hellinger–Reissner functional is adequate as a variational foundation, e.g. [3]. In case of nonlinear material behavior a local iteration for the determination of the physical strains is necessary [4]. Then a Hu–Washizu functional with independent displacements, stresses and strains is a proper alternative, e.g. [5–10]. In [7, 8] it is shown that these type of mixed elements show a superior convergence behavior in Newton' s method in comparison to standard displacement elements and standard enhanced elements. Very large load steps with essentially less iterations are possible. It should be noted that in this respect also measures can be taken to improve the robustness of displacement elements and enhanced strain elements, [11, 12].

Stabilization techniques based on a Taylor expansion of the shape functions and assumed strains have been used by Belytschko et al. [13, 14]. This initiated the development of a

✉ Werner Wagner
werner.wagner@kit.edu

Friedrich Gruttmann
gruttmann@mechanik.tu-darmstadt.de

1 Institut für Mechanik, Technische Universität Darmstadt, Franziska-Braun-Str. 7, 64287 Darmstadt, Germany

2 Institut für Baustatik, Karlsruhe Institute of Technology, Kaiserstr. 12, 76131 Karlsruhe, Germany

Published online: 30 July 2026

whole new class of under-integrated and hourglass stabilized finite elements. The elements are convergent since the stabilization forces are constructed orthogonal to the constant strain modes including rigid body motion. The underlying Hu-Washizu variational functional is applied in a special form. The assumed stress field is chosen orthogonal to the difference between the interpolated strain and the standard strain.

Element formulations with incompatible displacement modes have been introduced in [15, 16]. A variational foundation for these type of elements was laid in [17, 18] and led to the development of numerous so-called enhanced strain elements, e.g. [19, 20]. In [22, 23] it was noticed that the performance of mixed elements in large deformation problems is not always satisfactory. In particular, for compression problems, enhanced elements may behave sensitively and exhibit hourglass instabilities. Corresponding stabilization techniques have been developed. In several cases the measures lead to reduced integrated elements with an additional stabilization part. Further developments improved the element behavior essentially for finite deformation problems, e.g. [24–29]. Polytopal finite element formulations [30, 31] are based on the scaled boundary parametrization and allow the construction of interpolation functions on arbitrary polygonal domains.

Complex structures are preferably discretized with tetrahedral elements. As standard four-node tetrahedral elements lead to poor results for coarse meshes different techniques have been developed to improve the element behavior. Nodal averaging procedures are applied in [32–35]. Surface or volumetric bubble functions are added in the framework of mixed principles, e.g. [36–38]. Stabilized elements with non-local pressure are proposed in [39]. So called F-bar methods have been developed in [40, 41]. A stabilized Petrov-Galerkin formulation is basis of the element [42]. The alternative is to use 10-node tetrahedral elements, e.g. [43] for linear problems. In [44–46] the elements consist of an ensemble of four-node linear tetrahedrons. The authors of [47] propose Cosserat point elements for nonlinear isotropic materials. In the paper [48] a quasi-smooth manifold element is developed and applied to linear static problems. However, 10-node tetrahedra also display some weaknesses: e.g. the elements behave relative stiff in the analysis of thin structures subjected to bending loads.

The essential features and new aspects of present formulation are as follows:

(i) The variational formulation of present approach is based on a nonlinear Hu–Washizu functional with independent displacements, stresses and strains. The ansatz functions for the independent fields for 10–node tetrahedral elements are specified. With elimination of stress and strain parameters on element level a mixed-hybrid element is obtained.

(ii) The linear element stiffness matrix possesses with 6 zero eigenvalues the correct rank. The element fulfills the 3D patch test in the common linear form. A constant stress and strain state is also achieved for geometrical and material nonlinearity.

(iii) Several examples demonstrate the effective performance of the element in geometrical and material nonlinear applications. Finite strain incompressible material behavior, finite strain elasto-plasticity and thin structures subjected to bending with very large deformations are accounted for. The element is characterized by remarkable robustness. Very large load steps are possible. The number of iterations is much lower compared to standard displacement elements. This holds especially for thin structures.

2 Hu–Washizu variational formulation

The body of interest in the reference configuration is denoted by $\mathscr{B} \subset \mathbb{R}^3$, parametrized in $\mathbf{X} = X_i\,\mathbf{e}_i$ with the Cartesian basis $\mathbf{e}_i$ and the current configuration by $\mathscr{S} \subset \mathbb{R}^3$, parametrized in $\mathbf{x} = x_i\,\mathbf{e}_i$. The displacement field $\mathbf{u}$ follows with $\mathbf{u} = \mathbf{x} - \mathbf{X}$. The nonlinear deformation map $\boldsymbol{\varphi}_t : \mathscr{B} \to \mathscr{S}$ at time $t \in \mathbb{R}_+$ maps points $\mathbf{X} \in \mathscr{B}$ onto points $\mathbf{x} \in \mathscr{S}$. The deformation gradient $\mathbf{F}$ is defined by

$$\mathbf{F}(\mathbf{X}) := \operatorname{Grad} \boldsymbol{\varphi}_t(\mathbf{X}) \tag{1}$$

with $\det \mathbf{F}(\mathbf{X}) > 0$. The index notation of $\mathbf{F}$ reads $F_{ij} := \partial x_i / \partial X_j$.

The surface $\partial\mathscr{B}$ of the body is partitioned into two disjoined parts $\partial\mathscr{B} = \partial\mathscr{B}_u \cup \partial\mathscr{B}_t$ with $\partial\mathscr{B}_u \cap \partial\mathscr{B}_t = \emptyset$. The structure is loaded statically by body forces $\bar{\mathbf{f}}$ in $\mathscr{B}$ as well as by surface tractions $\bar{\mathbf{t}}$ on $\partial\mathscr{B}_t$. The loads are assumed to be independent of the displacements. Hence, the displacement boundary conditions and the stress boundary conditions read

$$\mathbf{u} = \bar{\mathbf{u}} \quad \text{on} \quad \partial\mathscr{B}_u \qquad \text{and} \qquad \mathbf{t} = \bar{\mathbf{t}} \quad \text{on} \quad \partial\mathscr{B}_t\,. \tag{2}$$

Present finite element formulation (FE) is based on a Hu–Washizu functional. Different pairs of work conjugate stress–strain measures could be used, e.g. the pair $\{\mathbf{P}, \mathbf{F}\}$, where $\mathbf{P}$ denotes the First Piola-Kirchhoff stress tensor. In present case we use the pair Second Piola-Kirchhoff stress tensor and Green-Lagrange strain tensor as the associated FE seems to be simpler. Let

$$\begin{aligned} \Pi(\mathbf{u}, \mathbf{S}, \mathbf{E}) = &\int_{\mathscr{B}} [W(\mathbf{E}) + \mathbf{S} : (\mathbf{E}_g(\mathbf{u}) - \mathbf{E}) - \mathbf{u} \cdot \bar{\mathbf{f}}]\,\mathrm{d}V \\ &- \int_{\partial\mathscr{B}_t} \mathbf{u} \cdot \bar{\mathbf{t}}\,\mathrm{d}A \to \text{stat.}\,, \end{aligned} \tag{3}$$

with the Green-Lagrange strain tensor

$$\mathbf{E}_g(\mathbf{u}) = \frac{1}{2}(\mathbf{F}^T\mathbf{F} - \mathbf{1})\,. \tag{4}$$

The index g refers to geometrical strains $\mathbf{E}_g$ as distinguished from the physical strains $\mathbf{E}_p = \mathbf{E}$. The Second Piola-Kirchhoff stresses $\mathbf{S}$ and the physical strains $\mathbf{E}$ are independent quantities of the functional. Existence of a strain energy density W as function of the physical strains $\mathbf{E}$ is assumed. Large strain polyconvex elasticity could be considered with the alternative use of the kinematic strains $\{\mathbf{F}, \mathbf{H}, J\}$ and their corresponding dual stresses. Here, $\mathbf{H}$ denotes the cofactor of $\mathbf{F}$ and $J = \det \mathbf{F}$, [49, 50].

Introducing $\boldsymbol{\theta} := [\mathbf{u}, \mathbf{S}, \mathbf{E}]^T$ and admissible variations $\delta\boldsymbol{\theta} := [\delta\mathbf{u}, \delta\mathbf{S}, \delta\mathbf{E}]^T$ the stationary condition associated with functional (3) reads with $\delta\mathbf{E}_g = \frac{1}{2}(\delta\mathbf{F}^T\mathbf{F} + \mathbf{F}^T\delta\mathbf{F})$

$$\begin{aligned} \delta\Pi &:= g(\boldsymbol{\theta}, \delta\boldsymbol{\theta}) \\ &= \int_{\mathscr{B}} [\delta\mathbf{E} : (\partial_{\mathbf{E}} W - \mathbf{S}) + \delta\mathbf{S} : (\mathbf{E}_g - \mathbf{E}) + \delta\mathbf{E}_g : \mathbf{S}]\, \mathrm{d}V \\ &\quad + g_{ext} = 0 \\ g_{ext} &= -\int_{\mathscr{B}} \delta\mathbf{u} \cdot \bar{\mathbf{f}}\, \mathrm{d}V - \int_{\partial\mathscr{B}_t} \delta\mathbf{u} \cdot \bar{\mathbf{t}}\, \mathrm{d}A\,. \end{aligned} \tag{5}$$

Application of the divergence theorem and standard arguments of variational calculus yields the associated Euler–Lagrange equations. These are the static and geometric field equations, the constitutive equations in $\mathscr{B}$, as well as the stress boundary conditions on $\partial\mathscr{B}_t$. The geometric boundary conditions have to be fulfilled as constraints.

The associated finite element equations are iteratively solved applying a Newton–Raphson iteration. For this purpose the linearization of the stationary condition (5) is expressed with $\mathbf{D} := \partial^2_{\mathbf{E}} W$ as

$$\begin{aligned} &\mathrm{L}[g(\boldsymbol{\theta}, \delta\boldsymbol{\theta}), \Delta\boldsymbol{\theta}] := g(\boldsymbol{\theta}, \delta\boldsymbol{\theta}) + \mathrm{D}g \cdot \Delta\boldsymbol{\theta} \\ &= g_{ext} + \int_{\mathscr{B}} \Delta\delta\mathbf{E}_g : \mathbf{S}\, \mathrm{d}V + \\ &\int_{\mathscr{B}} \begin{bmatrix} \delta\mathbf{E}_g \\ \delta\mathbf{S} \\ \delta\mathbf{E} \end{bmatrix} : \left\{ \begin{bmatrix} \mathbf{S} \\ \mathbf{E}_g - \mathbf{E} \\ \partial_{\mathbf{E}} W - \mathbf{S} \end{bmatrix} + \begin{bmatrix} \mathbf{0} & \mathbf{I} & \mathbf{0} \\ \mathbf{I} & \mathbf{0} & -\mathbf{I} \\ \mathbf{0} & -\mathbf{I} & \mathbf{D} \end{bmatrix} \begin{bmatrix} \Delta\mathbf{E}_g \\ \Delta\mathbf{S} \\ \Delta\mathbf{E} \end{bmatrix} \right\} \mathrm{d}V\,. \end{aligned} \tag{6}$$

Here, $\mathbf{I}$ denotes a fourth order unit tensor as well as $\Delta\mathbf{E}_g = \frac{1}{2}(\Delta\mathbf{F}^T\mathbf{F} + \mathbf{F}^T\Delta\mathbf{F})$ and $\Delta\delta\mathbf{E}_g = \frac{1}{2}(\delta\mathbf{F}^T\Delta\mathbf{F} + \Delta\mathbf{F}^T\delta\mathbf{F})$.

Remark: It is important to note that for inelastic material behavior Eq. (3) does not hold, whereas the successive ones are applicable. We keep the notation $\partial_{\mathbf{E}} W$ for the Second Piola-Kirchhoff stresses computed from the material law. They are obtained with the respective inelastic material law.

3 Finite element equations

In this section the finite element equations for ten-node tetrahedral elements are specified. Within the FE approximation the body is divided in element domains with $\mathscr{B} = \cup_{e=1}^{numel} \mathscr{B}_e$, where *numel* is the total number of elements. In the following component representations of vectors and tensors with respect to the fixed Cartesian basis $\mathbf{e}_i$ are specified. The isoparametric mapping is applied for the initial geometry $\mathbf{X} = X_i\, \mathbf{e}_i$ and the displacements $\mathbf{u} = u_i\, \mathbf{e}_i$

$$\mathbf{X}^h = \sum_{I=1}^{10} N_I(\boldsymbol{\xi})\,\mathbf{X}_I \qquad \mathbf{u}^h = \sum_{I=1}^{10} N_I(\boldsymbol{\xi})\,\mathbf{v}_I\,. \tag{7}$$

Here, $\mathbf{X}_I$ and $\mathbf{v}_I$ denote the vector of coordinates and displacements of node I, respectively. The superscript h refers to the characteristic size of the finite element discretization and indicates the finite element approximation. The numbering of the element nodes in the parameter space is given in Fig. 1. The shape functions N_I are formulated in terms of the natural coordinates $0 \le \boldsymbol{\xi} = \{\xi, \eta, \zeta\} \le 1$.

The virtual element displacements $\delta\mathbf{u}$ are interpolated with the same shape functions

$$\delta\mathbf{u}^h = \sum_{I=1}^{10} N_I(\boldsymbol{\xi})\,\delta\mathbf{v}_I\,, \tag{8}$$

where $\delta\mathbf{v}_I$ is the virtual element displacement vector of node I.

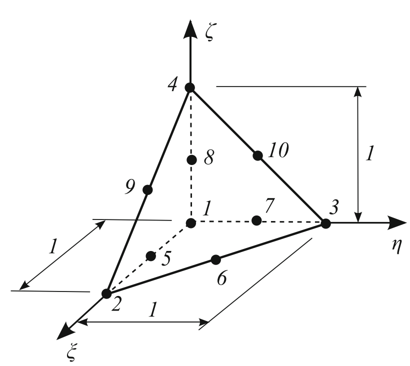

$$\begin{aligned} N_1 &= \kappa(2\kappa - 1) \\ N_2 &= \xi\,(2\xi - 1) \\ N_3 &= \eta\,(2\eta - 1) \\ N_4 &= \zeta\,(2\zeta - 1) \\ N_5 &= 4\xi\,\kappa \\ N_6 &= 4\xi\,\eta \\ N_7 &= 4\eta\,\kappa \\ N_8 &= 4\zeta\,\kappa \\ N_9 &= 4\xi\,\zeta \\ N_{10} &= 4\eta\,\zeta \\ \kappa &= 1 - \xi - \eta - \zeta \end{aligned}$$

Fig. 1 Shape functions of the ten-node tetrahedron element

Applying Voigt notation the FE approximation of the Green-Lagrange strain tensor reads

$$\mathbf{E}_g^h = \begin{bmatrix} E_{11}^h \\ E_{22}^h \\ E_{33}^h \\ 2E_{12}^h \\ 2E_{13}^h \\ 2E_{23}^h \end{bmatrix} = \begin{bmatrix} \frac{1}{2}\,(\mathbf{x}^h_{,1}\cdot\mathbf{x}^h_{,1} - 1) \\ \frac{1}{2}\,(\mathbf{x}^h_{,2}\cdot\mathbf{x}^h_{,2} - 1) \\ \frac{1}{2}\,(\mathbf{x}^h_{,2}\cdot\mathbf{x}^h_{,2} - 1) \\ \mathbf{x}^h_{,1}\cdot\mathbf{x}^h_{,2} \\ \mathbf{x}^h_{,1}\cdot\mathbf{x}^h_{,3} \\ \mathbf{x}^h_{,2}\cdot\mathbf{x}^h_{,3} \end{bmatrix} \tag{9}$$

with

$$\mathbf{x}^h_{,j} = \sum_{I=1}^{10} N_{I,j}\;(\mathbf{X}_I + \mathbf{v}_I) \qquad j = 1, 2, 3\,. \tag{10}$$

The shape function derivatives $N_{I,j}$ are computed in a standard way using the inverse of the Jacobian matrix $\mathbf{J}$, where

$$\mathbf{J} = \begin{bmatrix} \mathbf{X}^h_{,\xi}\cdot\mathbf{e}_1 & \mathbf{X}^h_{,\eta}\cdot\mathbf{e}_1 & \mathbf{X}^h_{,\zeta}\cdot\mathbf{e}_1 \\ \mathbf{X}^h_{,\xi}\cdot\mathbf{e}_2 & \mathbf{X}^h_{,\eta}\cdot\mathbf{e}_2 & \mathbf{X}^h_{,\zeta}\cdot\mathbf{e}_2 \\ \mathbf{X}^h_{,\xi}\cdot\mathbf{e}_3 & \mathbf{X}^h_{,\eta}\cdot\mathbf{e}_3 & \mathbf{X}^h_{,\zeta}\cdot\mathbf{e}_3 \end{bmatrix} \tag{11}$$

is obtained with $\mathbf{X}^h_{,\xi} = \sum_{I=1}^{10} N_{I,\xi}\;\mathbf{X}_I$ and analogous relations for $\mathbf{X}^h_{,\eta}$ and $\mathbf{X}^h_{,\zeta}$.

The finite element approximation of $\delta\boldsymbol{\theta}^h := [\delta\mathbf{E}_g^h, \delta\mathbf{S}^h, \delta\mathbf{E}^h]^T$ can be written as

$$\begin{bmatrix} \delta\mathbf{E}_g^h \\ \delta\mathbf{S}^h \\ \delta\mathbf{E}^h \end{bmatrix} = \begin{bmatrix} \mathbf{B} & \mathbf{0} & \mathbf{0} \\ \mathbf{0} & \mathbf{N}_\sigma & \mathbf{0} \\ \mathbf{0} & \mathbf{0} & \mathbf{N}_\varepsilon \end{bmatrix} \begin{bmatrix} \delta\mathbf{v} \\ \delta\hat{\boldsymbol{\sigma}} \\ \delta\hat{\boldsymbol{\varepsilon}} \end{bmatrix}$$
$$\delta\boldsymbol{\theta}^h = \mathbf{N}_\theta\,\delta\hat{\boldsymbol{\theta}} \tag{12}$$

with $\delta\mathbf{v} = [\delta\mathbf{v}_1, \ldots, \delta\mathbf{v}_I, \ldots, \delta\mathbf{v}_{10}]^T$. The submatrix of $\mathbf{B} = [\mathbf{B}_1, \ldots, \mathbf{B}_I, \ldots \mathbf{B}_{10}]$ for node I reads

$$\mathbf{B}_I = \begin{bmatrix} N_{I,1}\;\mathbf{x}^{hT}_{,1} \\ N_{I,2}\;\mathbf{x}^{hT}_{,2} \\ N_{I,3}\;\mathbf{x}^{hT}_{,3} \\ N_{I,1}\;\mathbf{x}^{hT}_{,2} + N_{I,2}\;\mathbf{x}^{hT}_{,1} \\ N_{I,1}\;\mathbf{x}^{hT}_{,3} + N_{I,3}\;\mathbf{x}^{hT}_{,1} \\ N_{I,2}\;\mathbf{x}^{hT}_{,3} + N_{I,3}\;\mathbf{x}^{hT}_{,2} \end{bmatrix}. \tag{13}$$

The matrix $\mathbf{N}_\sigma$ for the interpolation of $\mathbf{S}^h = \mathbf{N}_\sigma\,\hat{\boldsymbol{\sigma}}$ and $\delta\mathbf{S}^h = \mathbf{N}_\sigma\,\delta\hat{\boldsymbol{\sigma}}$ is chosen as

$$\mathbf{N}_\sigma = \left[\mathbf{N}_\sigma^1, \mathbf{N}_\sigma^2\right]$$
$$\mathbf{N}_\sigma^1 = \mathbf{1}_6 \qquad \mathbf{N}_\sigma^2 = \mathbf{M}(\boldsymbol{\xi}) \tag{14}$$

with the unit matrix $\mathbf{1}_n$ of order n and

$$\mathbf{M}(\boldsymbol{\xi}) = \begin{bmatrix} \xi\;\eta\;\zeta\;0\;0\;0\;0\;0\;0\;0\;0\;0\;0\;0\;0\;0\;0\;0 \\ 0\;0\;0\;\xi\;\eta\;\zeta\;0\;0\;0\;0\;0\;0\;0\;0\;0\;0\;0\;0 \\ 0\;0\;0\;0\;0\;0\;\xi\;\eta\;\zeta\;0\;0\;0\;0\;0\;0\;0\;0\;0 \\ 0\;0\;0\;0\;0\;0\;0\;0\;0\;\xi\;\eta\;\zeta\;0\;0\;0\;0\;0\;0 \\ 0\;0\;0\;0\;0\;0\;0\;0\;0\;0\;0\;0\;\xi\;\eta\;\zeta\;0\;0\;0 \\ 0\;0\;0\;0\;0\;0\;0\;0\;0\;0\;0\;0\;0\;0\;0\;\xi\;\eta\;\zeta \end{bmatrix}. \tag{15}$$

The vector $\hat{\boldsymbol{\sigma}} = [\hat{\boldsymbol{\sigma}}_1, \hat{\boldsymbol{\sigma}}_2]^T$ contains 6 parameters for the constant part and 18 parameters for the varying part of the stress approximation and analogously for $\delta\hat{\boldsymbol{\sigma}}$.

The matrix $\mathbf{N}_\varepsilon$ for the interpolation of the independent strains $\mathbf{E}^h = \mathbf{N}_\varepsilon\,\hat{\boldsymbol{\varepsilon}}$ and associated variation $\delta\mathbf{E}^h = \mathbf{N}_\varepsilon\,\delta\hat{\boldsymbol{\varepsilon}}$ is chosen as

$$\mathbf{N}_\varepsilon = \left[\mathbf{N}_\varepsilon^1, \mathbf{N}_\varepsilon^2\right]$$
$$\mathbf{N}_\varepsilon^1 = \mathbf{1}_6 \qquad \mathbf{N}_\varepsilon^2 = \mathbf{M}(\boldsymbol{\xi})\,. \tag{16}$$

For the parameter vector holds $\hat{\boldsymbol{\varepsilon}} = [\hat{\boldsymbol{\varepsilon}}_1, \hat{\boldsymbol{\varepsilon}}_2]^T$ with $\hat{\boldsymbol{\varepsilon}}_1 \in \mathbb{R}^6$, $\hat{\boldsymbol{\varepsilon}}_2 \in \mathbb{R}^{18}$, and analogously for $\delta\hat{\boldsymbol{\varepsilon}}$.

The finite element approximation of the virtual work of $\bar{\mathbf{f}}$ and $\bar{\mathbf{t}}$ leads to

$$g_{ext}^h = -\sum_{e=1}^{numel} \delta\mathbf{v}^T\,\mathbf{f}^a, \tag{17}$$

where $\mathbf{f}^a$ corresponds to the load vector of a standard 10-node tetrahedral element. Furthermore, it holds

$$\int_{\mathscr{B}} \Delta\delta\mathbf{E}_g^{hT}\,\mathbf{S}^h\,\mathrm{d}V = \sum_{e=1}^{numel} \delta\mathbf{v}^T\mathbf{K}_g\,\Delta\mathbf{v}$$
$$\mathbf{K}_g = \int_{\mathscr{B}_e} \mathbf{K}_\sigma(\mathbf{S}^h)\,\mathrm{d}V\,. \tag{18}$$

Let $\mathbf{K}_{IK} = \mathbf{N}_{IK}^T\mathbf{S}^h\,\mathbf{1}_3$ the submatrix of $\mathbf{K}_\sigma$ related to nodes $I, K \in \{1, \ldots, I, K, \ldots 10\}$ with

$$\mathbf{N}_{IK} = \begin{bmatrix} N_{I,1}\,N_{K,1} \\ N_{I,2}\,N_{K,2} \\ N_{I,3}\,N_{K,3} \\ N_{I,1}\,N_{K,2} + N_{I,2}\,N_{K,1} \\ N_{I,1}\,N_{K,3} + N_{I,3}\,N_{K,1} \\ N_{I,2}\,N_{K,3} + N_{I,3}\,N_{K,2} \end{bmatrix} \qquad \mathbf{S}^h = \begin{bmatrix} S^{11} \\ S^{22} \\ S^{33} \\ S^{12} \\ S^{13} \\ S^{23} \end{bmatrix}. \tag{19}$$

We insert $\delta\boldsymbol{\theta}^h = \mathbf{N}_\theta\,\delta\hat{\boldsymbol{\theta}}$ according to Eq. (12) and the corresponding equation $\Delta\boldsymbol{\theta}^h = \mathbf{N}_\theta\,\Delta\hat{\boldsymbol{\theta}}$ along with Eqs. (17)

and (18) into the linearized variational Eq. (6) and obtain

$$
\begin{aligned}
&\mathrm{L}\,[g(\boldsymbol{\theta}^h, \delta\boldsymbol{\theta}^h), \Delta\boldsymbol{\theta}^h] \\
&= \sum_{e=1}^{numel} \begin{bmatrix} \delta\mathbf{v} \\ \delta\hat{\boldsymbol{\sigma}} \\ \delta\hat{\boldsymbol{\varepsilon}} \end{bmatrix}_e^T \left\{ \begin{bmatrix} \mathbf{f}^i - \mathbf{f}^a \\ \mathbf{f}^s \\ \mathbf{f}^e \end{bmatrix} + \begin{bmatrix} \mathbf{K}_g & \mathbf{G}^T & \mathbf{0} \\ \mathbf{G} & \mathbf{0} & \mathbf{L}^T \\ \mathbf{0} & \mathbf{L} & \mathbf{H} \end{bmatrix} \begin{bmatrix} \Delta\mathbf{v} \\ \Delta\hat{\boldsymbol{\sigma}} \\ \Delta\hat{\boldsymbol{\varepsilon}} \end{bmatrix} \right\}_e
\end{aligned} \tag{20}
$$

with

$$
\begin{aligned}
\mathbf{f}^i &= \int_{\mathcal{B}_e} \mathbf{B}^T \mathbf{S}^h \; \mathrm{d}V = \mathbf{G}^T \hat{\boldsymbol{\sigma}} & \mathbf{L} &= -\int_{\mathcal{B}_e} \mathbf{N}_\varepsilon^T \, \mathbf{N}_\sigma \; \mathrm{d}V \\
\mathbf{f}^s &= \int_{\mathcal{B}_e} \mathbf{N}_\sigma^T \, \mathbf{E}_g^h \; \mathrm{d}V + \mathbf{L}^T \hat{\boldsymbol{\varepsilon}} & \mathbf{G} &= \int_{\mathcal{B}_e} \mathbf{N}_\sigma^T \, \mathbf{B} \; \mathrm{d}V \\
\mathbf{f}^e &= \int_{\mathcal{B}_e} \mathbf{N}_\varepsilon^T \, \partial_{\mathbf{E}} W \; \mathrm{d}V + \mathbf{L}\,\hat{\boldsymbol{\sigma}} & \mathbf{H} &= \int_{\mathcal{B}_e} \mathbf{N}_\varepsilon^T \, \mathbf{D}\, \mathbf{N}_\varepsilon \; \mathrm{d}V\,.
\end{aligned} \tag{21}
$$

For all integrals, an 11-point modified Newton Cotes integration scheme with strictly positive weights and an order of accuracy of four is employed, [51]. The integration points are the 10 nodes and the center of gravity with coordinates $\boldsymbol{\xi}_{11} = \{1/4, 1/4, 1/4\}$. The associated weights are $w_i = 1/360$, i =1-4; $w_i = 4/360$, i =5-10 and $w_{11} = 32/360$. Further integration schemes can be found e.g. in [52, 53] among others.

Let $\mathrm{L}[g(\boldsymbol{\theta}^h, \delta\boldsymbol{\theta}^h), \Delta\boldsymbol{\theta}^h] = 0$ with $[\delta\mathbf{v}, \delta\hat{\boldsymbol{\sigma}}, \delta\hat{\boldsymbol{\varepsilon}}]_e^T \neq \mathbf{0}$. One obtains for each element the set of equations

$$
\begin{bmatrix} \mathbf{K}_g & \mathbf{G}^T & \mathbf{0} \\ \mathbf{G} & \mathbf{0} & \mathbf{L}^T \\ \mathbf{0} & \mathbf{L} & \mathbf{H} \end{bmatrix} \begin{bmatrix} \Delta\mathbf{v} \\ \Delta\hat{\boldsymbol{\sigma}} \\ \Delta\hat{\boldsymbol{\varepsilon}} \end{bmatrix} + \begin{bmatrix} \mathbf{f}^i - \mathbf{f}^a \\ \mathbf{f}^s \\ \mathbf{f}^e \end{bmatrix} = \begin{bmatrix} \mathbf{r} \\ \mathbf{0} \\ \mathbf{0} \end{bmatrix}. \tag{22}
$$

At equilibrium states holds $\mathbf{f}^s = \mathbf{f}^e = \mathbf{0}$. The vector of element nodal forces $\mathbf{r}$ cancels out with the assembly.

Since the stresses and strains are interpolated discontinuously across the element boundaries the parameter vectors $\Delta\hat{\boldsymbol{\varepsilon}}$ and $\Delta\hat{\boldsymbol{\sigma}}$ can be eliminated from the set of equations

$$
\begin{aligned}
\Delta\hat{\boldsymbol{\sigma}} &= -\mathbf{L}^{-1} \,(\mathbf{H}\, \Delta\hat{\boldsymbol{\varepsilon}} + \mathbf{f}^e) \\
\Delta\hat{\boldsymbol{\varepsilon}} &= -\mathbf{L}^{-T} \,(\mathbf{G}\, \Delta\mathbf{v} + \mathbf{f}^s)\,.
\end{aligned} \tag{23}
$$

Inserting (23) into (22) leads to $\mathbf{K}_T^e \, \Delta\mathbf{v} + \hat{\mathbf{f}} = \mathbf{r}$ and thus the tangential element stiffness matrix $\mathbf{K}_T^e$ and the element residual vector $\hat{\mathbf{f}}$

$$
\begin{aligned}
\mathbf{K}_T^e &= \mathbf{G}^T \, \hat{\mathbf{H}}\, \mathbf{G} + \mathbf{K}_g \\
\hat{\mathbf{f}} &= \mathbf{G}^T \,(\hat{\boldsymbol{\sigma}} + \hat{\mathbf{H}}\, \mathbf{f}^s - \mathbf{L}^{-1}\, \mathbf{f}^e) - \mathbf{f}^a \\
\hat{\mathbf{H}} &= \mathbf{L}^{-1}\, \mathbf{H}\, \mathbf{L}^{-T}
\end{aligned} \tag{24}
$$

Table 1 Used element labels

H27	27-node hexahedral displacement element with quadratic displacements
T10	10-node tetrahedral displacement element with quadratic displacements
HWT10	Present 10-node Hu-Washizu tetrahedral element

The linear element stiffness matrix possesses with six zero eigenvalues the correct rank. The update of the parameter vectors $\hat{\boldsymbol{\sigma}} \Leftarrow \hat{\boldsymbol{\sigma}} + \Delta\hat{\boldsymbol{\sigma}}$ with $\Delta\hat{\boldsymbol{\sigma}} = [\Delta\hat{\boldsymbol{\sigma}}_1, \Delta\hat{\boldsymbol{\sigma}}_2]^T$ and $\hat{\boldsymbol{\varepsilon}} \Leftarrow \hat{\boldsymbol{\varepsilon}} + \Delta\hat{\boldsymbol{\varepsilon}}$ with $\Delta\hat{\boldsymbol{\varepsilon}} = [\Delta\hat{\boldsymbol{\varepsilon}}_1, \Delta\hat{\boldsymbol{\varepsilon}}_2]^T$ is performed using Eq. (23). For this purpose the necessary matrices have to be stored or to be recomputed.

4 Examples

The derived element formulation is implemented in an extended version of the general purpose finite element program FEAP [51]. In the tables and diagrams below the solutions are labeled with abbreviations according to Table 1.

4.1 The patch test

The patch test, as is defined in Ref. [37], is considered first. Figure 2 shows a distorted hexahedral patch composed of 6 ten-noded tetrahedral elements. The coordinates of the nodes 1 to 27 are specified below. Linear, elastic isotropic material behavior with Young's modulus $E = 1000$ N/mm^2 and Poisson's ratio $\nu = 0.3$ is assumed.

According to Ref. [54] the test is performed in two parts. In the first part (Test A) displacements

$$
u_x = \varepsilon_x \, x \qquad u_y = \varepsilon_y \, y \qquad u_z = \varepsilon_z \, z\,. \tag{25}
$$

are applied at all nodes with the nodal coordinates x, y, z, except the central node 14. They are obtained with the strains via the material law and $\sigma_x = 2$ N/mm^2, $\sigma_y = 0$, $\sigma_z = 0$

$$
\begin{aligned}
\varepsilon_x &= \frac{1}{E}(\sigma_x - \nu(\sigma_y + \sigma_z)) = \frac{\sigma_x}{E} = 0.002 \\
\varepsilon_y &= \frac{1}{E}(\sigma_y - \nu(\sigma_x + \sigma_z)) = -\nu\,\frac{\sigma_x}{E} = -0.0006 \\
\varepsilon_z &= \frac{1}{E}(\sigma_z - \nu(\sigma_x + \sigma_y)) = -\nu\,\frac{\sigma_x}{E} = -0.0006\,.
\end{aligned} \tag{26}
$$

For the linear patch test the symbols ε and σ replace the nonlinear strains E and stresses S. Hence, the remaining displacements of node 14 are computed. The subsequent stress computation leads at all Gauss points the constant stress state $\sigma_x = 2$ N/mm^2, $\sigma_y = 0$, $\sigma_z = 0$, see Fig. 3 for σ_x. Additional, the nodal forces F_x obtained from the finite element

Fig. 2 Distorted hexahedral patch, nodal coordinates, displacements and forces

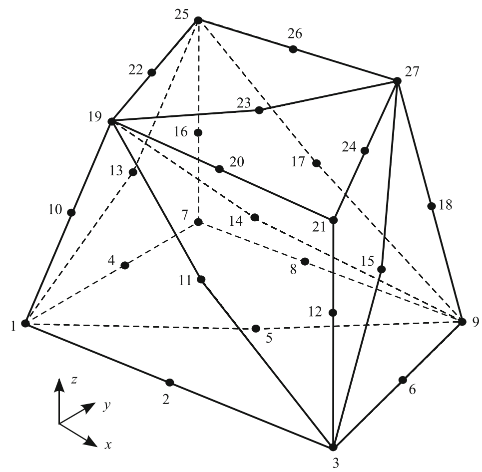

Node	x	y	z	u_x	u_y	$12 \cdot F_x$
1	1.5000	1.0000	0.0000	0.003		
2	3.0000	1.2500	0.0000			3.6
3	4.5000	1.5000	0.0000	0.009	−0.0009	
4	1.5000	2.0000	0.0000			−16.6
5	2.8750	2.2500	0.0000			
6	4.2500	2.5000	0.0000			17.1
7	1.5000	3.0000	0.0000			−0.65
8	2.7500	3.2500	0.0000			−5.
9	4.0000	3.5000	0.0000			0.525
10	1.7500	1.2500	1.0000			−8.2
11	3.0625	1.4375	1.0000			6.
12	4.3750	1.6250	1.0000			15.7
13	1.7500	2.0000	1.1250			−27.
14	2.9375	2.2188	1.1250			
15	4.1250	2.4375	1.1250			29.5
16	1.7500	2.7500	1.2500			−20.6
17	2.8125	3.0000	1.2500			−10.
18	3.8750	3.2500	1.2500			11.6
19	2.0000	1.5000	2.0000			0.275
20	3.1250	1.6250	2.0000			3.
21	4.2500	1.7500	2.0000			−0.65
22	2.0000	2.0000	2.2500			−9.6
23	3.0000	2.1875	2.2500			1.5
24	4.0000	2.3750	2.2500			13.1
25	2.0000	2.5000	2.5000			0.775
26	2.8750	2.7500	2.5000			−4.1
27	3.7500	3.0000	2.5000			−0.3

Fig. 3 Patch test: displacements u_x and stresses σ_x

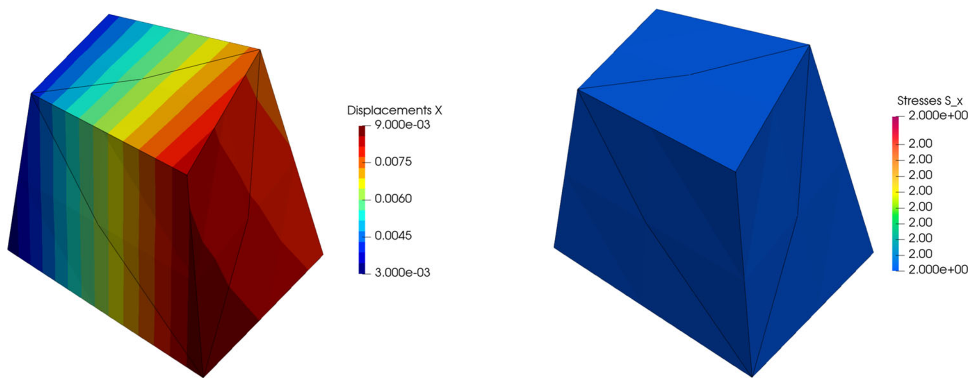

calculation are summarized in Fig. 2. The other components F_y, F_z are zero.

In the second part (Test C) the displacements u_z of nodes 1-9 are set to zero, nodes 1 and 3 are bounded in x-direction and node 3 in y-direction with values u_x, u_y according to Fig. 2. Furthermore, forces F_x are prescribed at the remaining nodes. With this loading the displacements and stresses are computed. The components u_x and σ_x are plotted in Fig. 3. The obtained constant stress state $\sigma_x = 2\ \mathrm{N/mm}^2, \sigma_y = 0, \sigma_z = 0$ confirms that present element fulfills the patch test.

Finally, we perform the test considering geometrical and material nonlinear behavior with the Neo-Hooke strain energy density

$$W(\mathbf{C}) = \frac{\mu}{2}(\mathrm{tr}\,\mathbf{C} - 3 - \ln(\det \mathbf{C})) + \frac{\lambda}{4}(\det \mathbf{C} - 1 - \ln(\det \mathbf{C}))\,, \tag{27}$$

where $\mathbf{C} = 2\,\mathbf{E} + \mathbf{1}$ is computed with the physical strains. The Lamé parameters λ and μ are chosen such that they correspond to the elasticity constants E and ν mentioned above. The test is again performed in two steps in an analogues way.

In both cases, with prescribed displacements and prescribed associated nodal forces, a constant stress state is obtained.

4.2 Block under constant partial load: quasi incompressible elastic solution

In this benchmark, a block with length $l = 50$ mm is subject to a load on part of its upper surface, see Fig. 4. Only one quarter is considered taking symmetry conditions into account. The constant load $q = 9\ \mathrm{N/mm}^2$ acts on the upper surface in negative z-direction.

The displacement boundary conditions and symmetry conditions are:

$$\begin{aligned} &u_z(x,y,0) = 0 \qquad u_x(0,y,z) = 0 \\ &u_x(x,y,l) = 0 \qquad u_y(x,0,z) = 0 \\ &u_y(x,y,l) = 0. \end{aligned} \tag{28}$$

The material behavior is described by a Neo-Hookean model with the strain energy function (27). The material parameters $\lambda = 499.92568\ \mathrm{N/mm}^2$ and $\mu = 1.61148\ \mathrm{N/mm}^2$ are taken from Ref. [55]. With $\lambda \gg \mu$ quasi incompressible material behavior is accounted for. The shaded quarter of the structure is discretized with a regular $N \times N \times N$ mesh, where

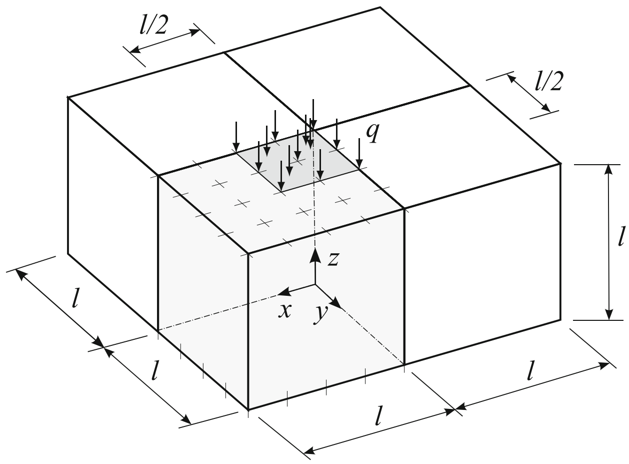

Fig. 4 Block under constant partial load

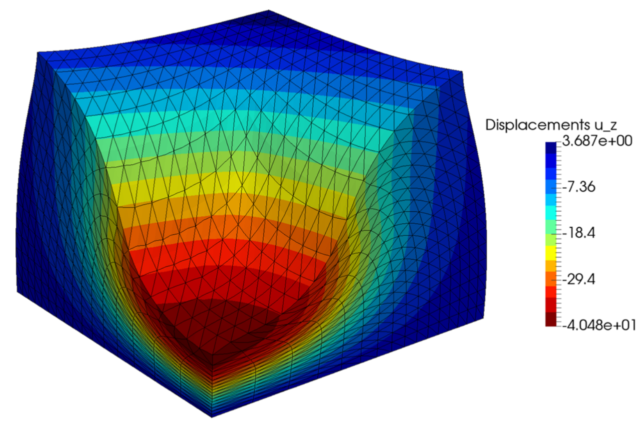

Fig. 6 Deformed block with displacements u_z for $q = 9\ \text{N/mm}^2$

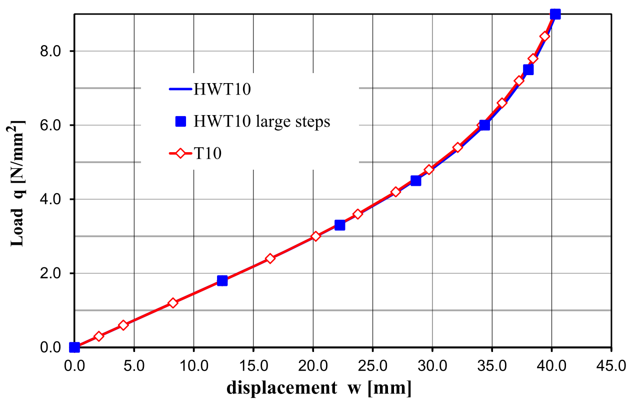

Fig. 5 Load q versus displacement w

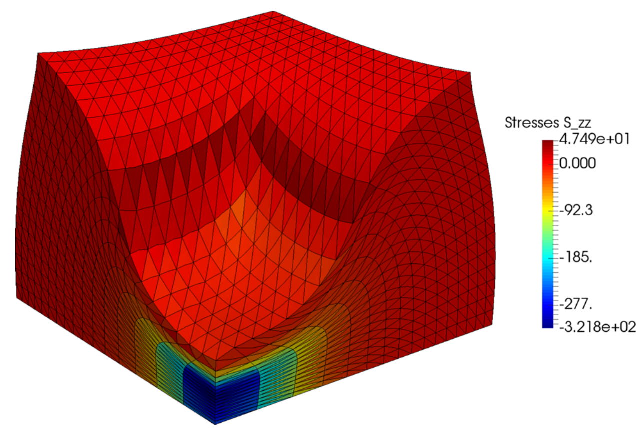

Fig. 7 Deformed block with stresses S_{zz} (not averaged) for $q = 9\ \text{N/mm}^2$

N denotes the number of hexahedral cells in the respective direction. Each cell is discretized with 6 ten-noded tetrahedral elements.

In Fig. 5 we compare the load deflection curves computed with the elements HWT10 and T10 using a mesh density $N = 16$. The applied load q is plotted versus the computed displacement $w = -u_z(0, 0, l)$. The solutions of the two elements agree with each other. With element T10 16 load steps are necessary to apply the total load $q = 9\ \text{N/mm}^2$. In contrast, with present element HWT10 the load can be applied in only 6 steps.

The deformed mesh with a plot of the displacements u_z is depicted in Fig. 6. The maximum compression amounts to approximately 80%. Furthermore, in Fig. 7 the stresses S_{zz} are plotted on the deformed mesh.

4.3 Block under constant partial load: elasto-plastic solution

In this example we investigate the behavior of the block according to Fig. 4, now for finite strain isotropic elasto-plasticity. The model of Simo [56], based on a multiplicative elasto-plastic split, a Hencky elastic law and von Mises yield condition with nonlinear isotropic hardening, is applied. The elasticity data λ and μ and the parameters of the hardening function $Y(\alpha) = Y_\infty + (Y_0 - Y_\infty)\exp[-\delta\,\alpha] + H\,\alpha$ according to Ref. [26] are given in Eq. (29). In this context, α denotes the equivalent plastic strains.

$$
\begin{aligned}
\lambda &= 110.8\ \ \text{N/mm}^2 & Y_0 &= 0.45\ \ \ \text{N/mm}^2 \\
\mu &= \ \ 80.2\ \ \text{N/mm}^2 & Y_\infty &= 0.715\ \ \text{N/mm}^2 \\
& & H &= 0.129\ \ \text{N/mm}^2 \\
& & \delta &= 16.93
\end{aligned}
\tag{29}
$$

The computations are performed with regular $8 \times 8 \times 8$ meshes, where again each cell is discretized with 6 ten-noded tetrahedral elements. We apply the arc length method with displacement control and step size $\Delta w = 1$ mm. To capture the start of plastification, four steps with increments $\Delta w = 0.25$ mm are calculated first. The loading path is computed up to $w = 25$ mm. Subsequently the structure is unloaded. In Fig. 8 the load displacement curves are depicted.

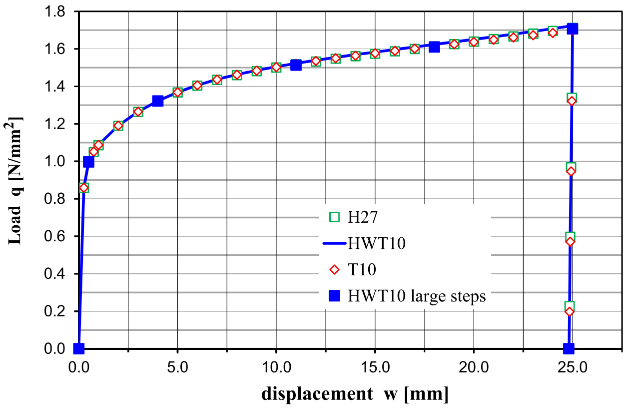

Fig. 8 Load q versus displacement w

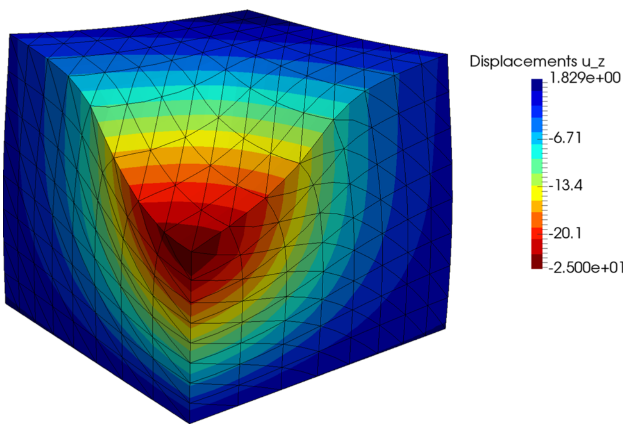

Fig. 9 Deformed block with displacements u_z at $w = 25$ mm

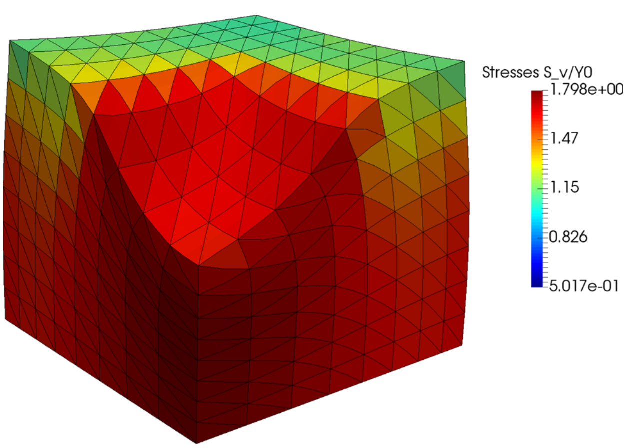

Fig. 10 Deformed block with σ_v/Y_0 (not averaged) at $w = 25$ mm

As can be seen there is agreement between the results of the elements H27, T10 and HWT10. Present element HWT10 allows a solution with very large load steps. The loading and unloading path can be traced with 6 steps in total. The final deformed mesh with a plot of the displacements u_z is shown in Fig. 9. The normalized von Mises stresses σ_v/Y_0 are shown in Fig. 10.

Table 2 Load q ($w = 25$ mm)

Mesh	Fig. 11 (top)	Fig. 11 (bottom)	Regular
q [N/mm^2]	1.726*	1.722	1.724

*averaged from 5 random discretizations

We also consider distorted $8 \times 8 \times 8$ meshes. In Fig. 11 (top), modified coordinates $X_{ik} \Leftarrow X_{ik} + 2 \cdot (r_{ik} - 0.5) \cdot l/50$ of a node k are computed using random numbers r_{ik}. These are obtained with the Fortran routine random_number() which returns for every run new random numbers from the uniform distribution over the range $0 \leq r_{ik} < 1$. The upper surface of the block is meshed regularly to allow for the loading. In Fig. 11 (bottom), the marked diagonally opposite nodes of the vertical edges are shifted to $X_3 = l/3$ and $X_3 = 2l/3$ respectively. The coordinates of the remaining nodes follow with the applied quadratic mapping. The coordinates X_1 and X_2 remain unchanged. With the distorted meshes the load deflection behavior is examined with element HWT10 again. The computed loads q for a prescribed displacement $w = 25$ mm are listed in Table 2. The associated curves are not displayed in Fig. 8 as differences in comparison with the results of the regular mesh are not visible.

4.4 Conical shell

This example is selected to demonstrate the ability of the developed finite element to deal with strongly nonlinear situations. The geometrical data are taken from Başar and Itskov [57]. There, the authors take with Ogden's material law elastic material behavior into account. Here, elasto-plasticity with nonlinear isotropic hardening is considered. Again the above mentioned finite strain model [56] is applied. All necessary material and geometrical data are depicted in Fig 12.

Considering symmetry conditions, only a quarter of the shell is discretized with a regular $8 \times 8 \times 1$ mesh of hexahedral cells. Each cell is subdivided by 6 ten-noded tetrahedral elements. That is, the structure can only snap through symmetrically. The load deflection curves are computed using the arc length method with control of the vertical displacements w of the loading point, see Fig. 13. At a displacement $w = 0.04$ a first limit point is reached. Then a rolling process starts at the top edge of the shell. Further stability points are traced at $w = 0.49$ (minimum) and $w = 1.26$ (maximum). A further local minimum of the load deflection curve is attained at $w = 1.77$. Subsequently a stable path with increasing loads arises. Finally, a total snap through of the shell is attained. There is good agreement between the solutions obtained with the elements HWT10 and T10. The element HWT10 allows a solution with very large load steps, which is also included

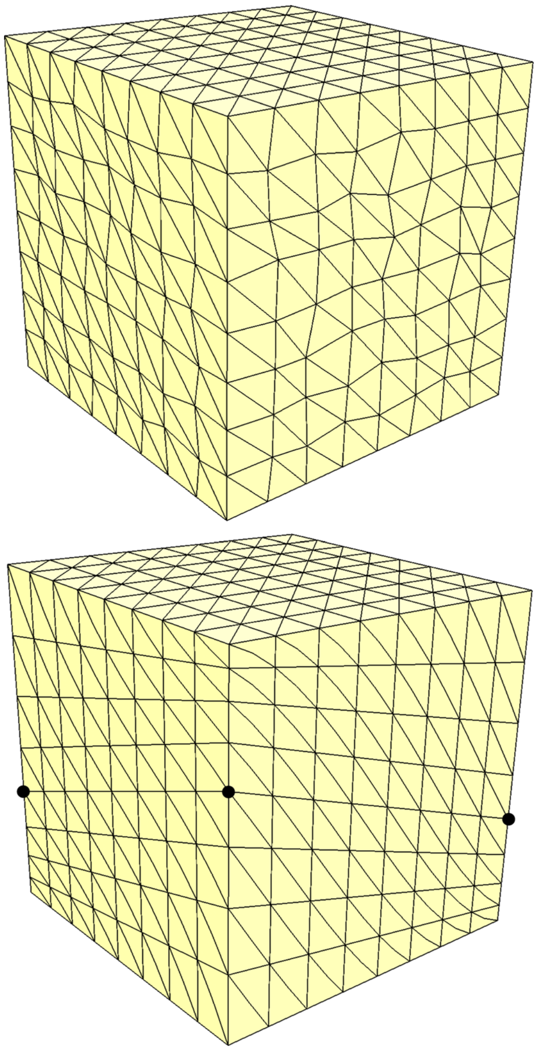

Fig. 11 Distorted $8 \times 8 \times 8$ meshes: distortion with random numbers (top) and distortion with nodal shift (bottom)

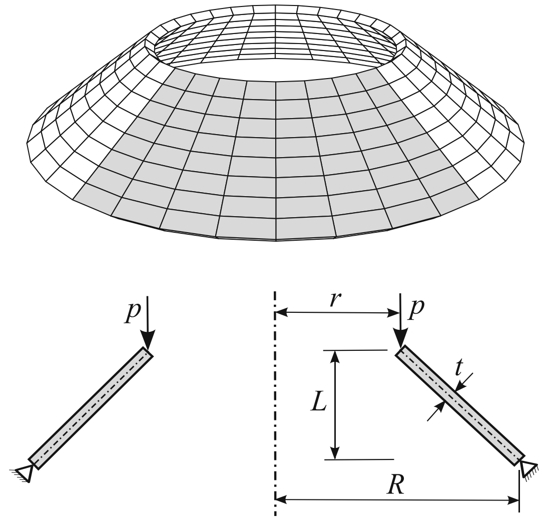

Geometry	Material		
$r = 1$	$\lambda = 110.8$	$Y_0 =$	0.45
$R = 2$	$\mu =$ 80.2	$Y_\infty =$	0.715
$L = 1$		$H =$	0.129
$t = 0.1$		$\delta =$	16.93

Fig. 12 Finite element mesh with geometrical and material data

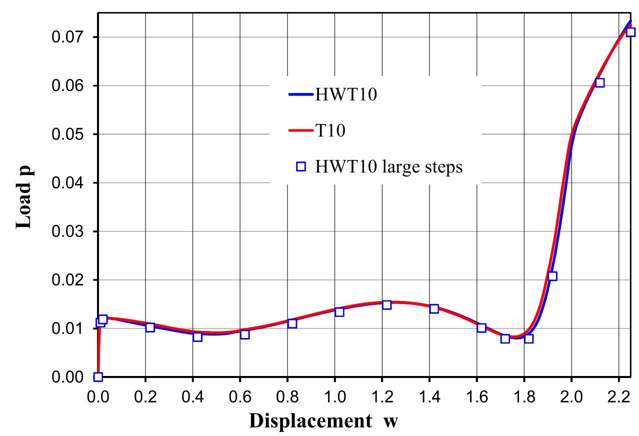

Fig. 13 Load deflection curves for a $8 \times 8 \times 1$ mesh

in Fig. 13. The deformed meshes at characteristic points are shown in Fig. 14.

This example could also be computed using 8-node solid shell elements. For example, in Ref. [8] this is done with one element in thickness direction and eccentric boundary conditions.

4.5 Annular plate

This example, which is shown in Fig. 15, has been introduced by Başar and Ding [58], see also Buechter and Ramm [59]. The annular plate is clamped at the slit. At the opposite surface of the slit acts a uniformly distributed load with a resultant p through the thickness. The material behavior of the homogeneous plate is described by the Saint Venant-Kirchhoff model with elasticity constants E and ν.

The plate is very thin with the ratio $R_2/h = 333$. The analysis is based on $N \times 8\,N \times 1$ meshes, where N denotes the number of hexahedral cells in radial direction and $8\,N$ in circumferential direction. Each cell is discretized with 6 ten-noded tetrahedral elements (Fig. 16).

The convergence behavior of the displacement $u_{zB} = u_z(R_2, 0, h/2)$ for the total load $p = 6$ versus N using the elements T10 and HWT10 is depicted in Fig. 17. One can see that present element yields a faster convergence behavior. With $N = 20$ one obtains practically the converged solution. Figure 18 shows that the load deflection curves of both elements agree with each other for the finest mesh density.

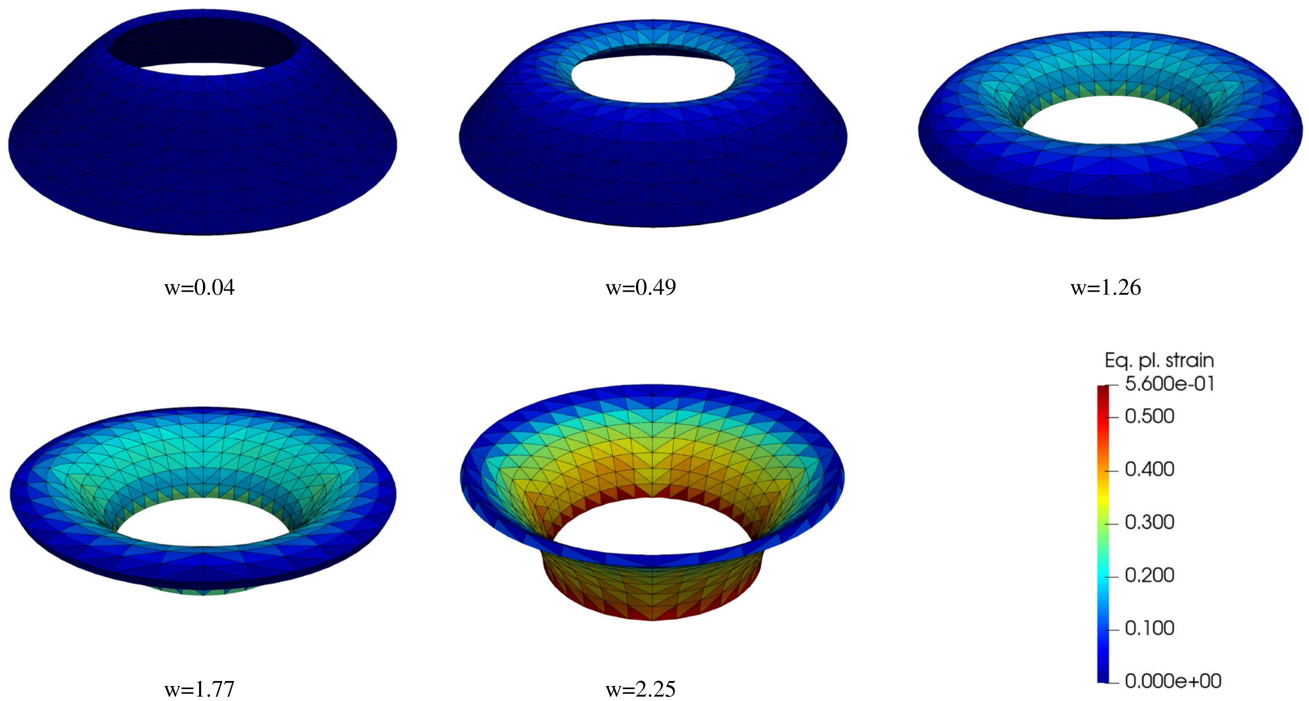

Fig. 14 Deformed meshes with a plot of the equivalent plastic strains (not averaged)

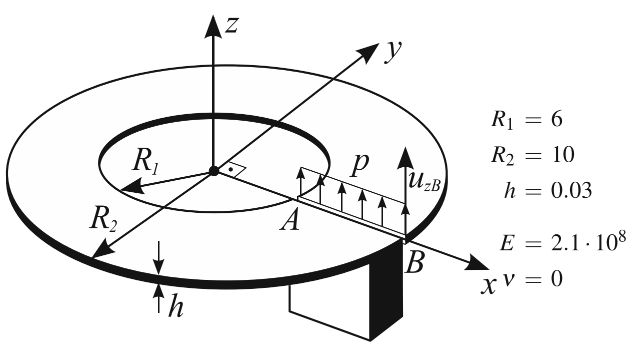

Fig. 15 Annular plate (not to scale): geometrical and material data

A comparative solution is computed with a 8×64 mesh of 4-node shell elements [60]. The associated load deflection curve is not plotted in Fig. 18 as differences to the depicted curves are not visible.

The following investigations are performed with the mesh density $N = 20$. The iteration behavior of displacement element T10 is documented in Table 3. When choosing 10 load steps of different step sizes Δp, then n iterations are necessary for convergence in the respective load step, hence in total 141 iterations. In contrast to that present element HWT10 allows the application of one single load step $\Delta p = 6$ with 10 iterations. This is proved by means of the norm of the global residual vector $||\mathbf{R}||$ in Table 4 and Fig. 18. The deformed plate with a plot of the displacements u_z for the final load $p = 6$ using a $8 \times 64 \times 1$ mesh is depicted in Fig. 19.

Table 3 Iteration behavior of element T10

load step	Δp	n
1	0.3	15
2	0.3	15
3	0.3	16
4	0.3	13
5	0.6	22
6	0.6	13
7	0.6	10
8	1.0	12
9	1.0	12
10	1.0	13
$\sum$	6	141

Table 4 Iteration behavior of element HWT10 for one single load step $\Delta p = 6$

iteration	$\|\|\mathbf{R}\|\|$
1	2.8142495E+00
2	7.8760257E+09
3	1.1019768E+09
4	1.5273548E+08
5	2.3918283E+07
6	2.3673903E+06
7	1.0798975E+05
8	7.2162681E+03
9	1.5324197E+01
10	4.0388697E-04

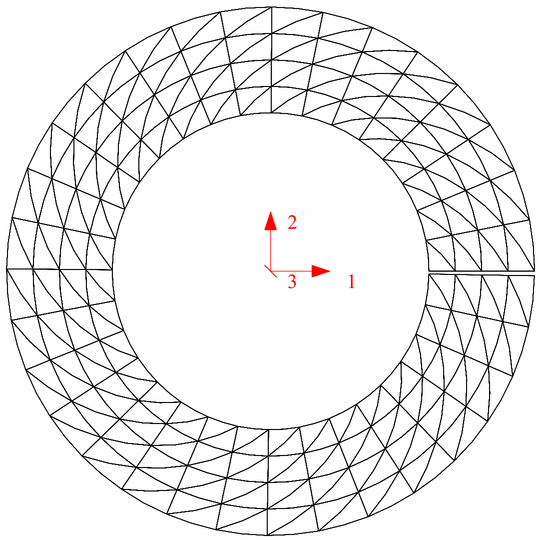

Fig. 16 Annular plate: mesh with 768 ten-node tetrahedral elements (N=4)

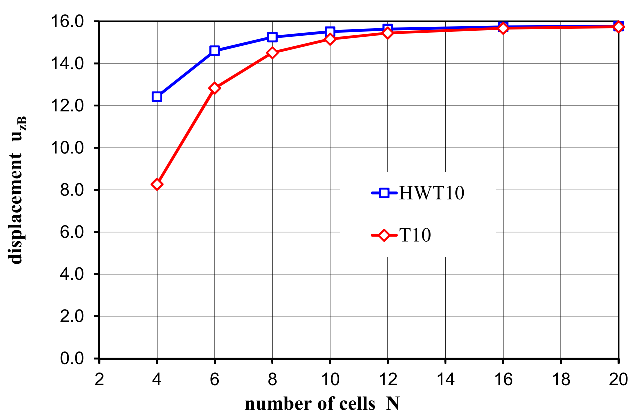

Fig. 17 Displacements $u_{zB}(p = 6)$ versus N

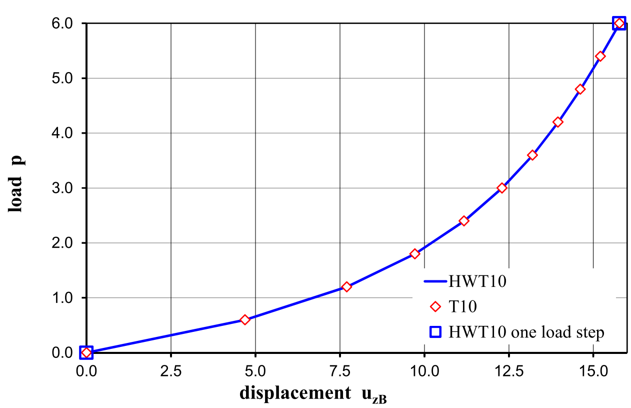

Fig. 18 Load deflection curves of the converged solutions

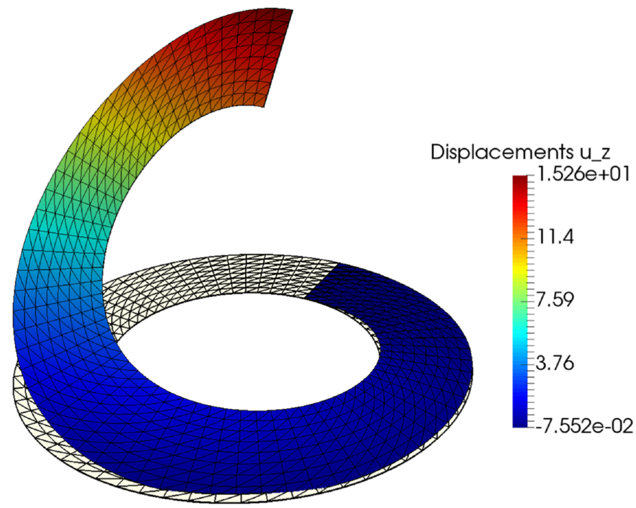

Fig. 19 Deformed plate at $p = 6$ with displacements u_z

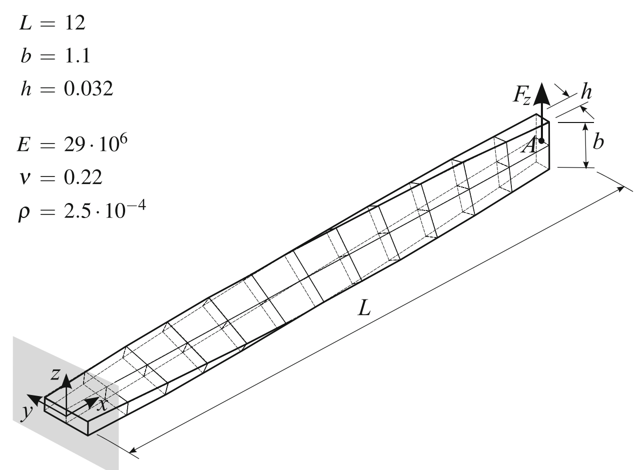

Fig. 20 Twisted beam (not to scale): geometrical and material data

4.6 Twisted beam: Dynamics

The cantilever with a 90° twist according to Fig. 20 consists of linear elastic material. This test example applying static loads was introduced in Ref. [61]. In present case the thickness is reduced by a factor 10. Hence, with a length-to-thickness ratio $L/h = 375$, it is a very thin structure. A time-constant load with a resultant $F_z(t) = 0.1$ is uniformly distributed at the free end. The analysis is based on meshes with $N \times 6\,N \times 1$ hexahedral cells, where N denotes the number of cells in transverse direction and $6\,N$ in length direction, see Fig. 20 for a $2 \times 12 \times 1$ mesh along with the geometrical and material data. Each cell is discretized with 6 ten-noded tetrahedral elements.

The extension of the finite element formulation for dynamical loads is a standard procedure. The variation of the Lagrange function $L = T - V$ must be zero within the time

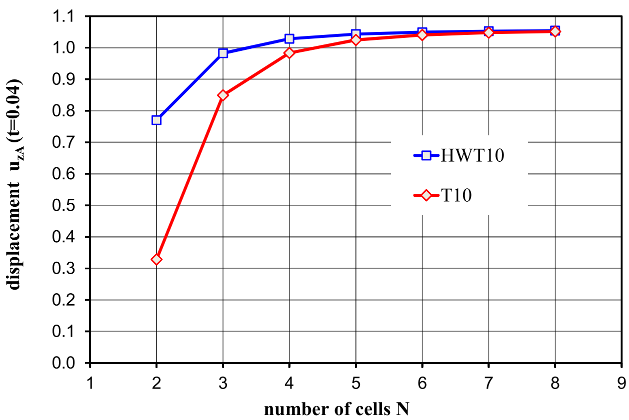

Fig. 21 Twisted beam: $u_{zA}(t = 0.04) - N$

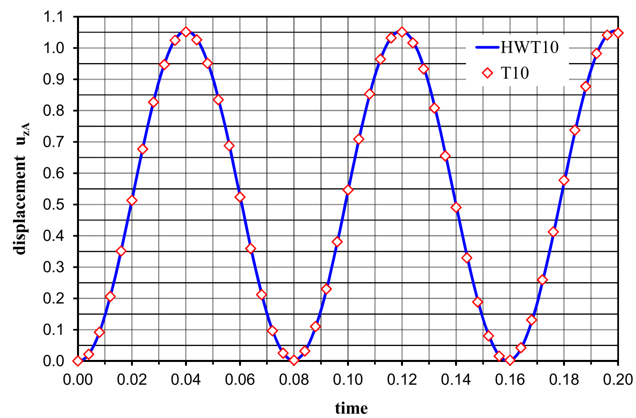

Fig. 22 Twisted beam (N=8): $u_{zA} - t$

range

$$\delta I = \delta \int_0^t L \, \mathrm{d}\bar{t} = 0 \,. \tag{30}$$

Here, T denotes the kinetic energy and V is the total potential energy according to Eq. (3). After variation and subsequent partial integration with respect to the time the variational form including the inertia terms follows. Introducing the shape functions for displacements, stresses and strains as well as the assembly, one ends up with a system of equations for the unknown discrete displacements, velocities and accelerations. Out of the field of time integration schemes we use Newmark's method. A constant time step $\Delta T = 1 \cdot 10^{-3}$ is chosen.

The geometrical linear computations are performed using present element HWT10 and the element T10. In Fig. 21 the displacements u_z of point A at time $t = 0.04$ are plotted versus the number of cells N in transverse direction. The mixed element HWT10 reveals a faster convergence behavior. With $N = 8$ one obtains practically the converged solution. Figure 22 shows that the displacement time curves of both elements agree with each other for a mesh density $N = 8$. With standard parameters $\gamma = 1/2$ and $\beta = 1/4$ as well as geometrical linearity Newmark's method is energy conserving. Thus the amplitude of the displacement is constant over time, see Fig. 22. In case of large deformation problems corresponding Hu-Washizu mixed variational formulations and their conservation law counterparts in dynamics have been developed e.g. in [62, 63].

4.7 Aluminum connector of a tensegrity tower

In the context of the last example, we examine an aluminum connector of a tensegrity tower for the German Museum in Munich. A detailed description of the project is presented in

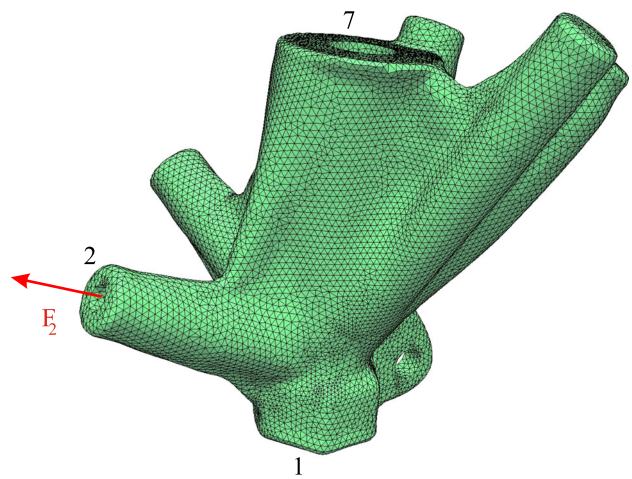

Fig. 23 FE-discretization of a 3D-node of a Tensegrity tower

[64, 65]. The CAD model of a 3D-node at a high point of the structure was kindly provided by Florian Oberhaidinger and Martin Mensinger, co-authors of [64]. Our former colleague Patrick Weber, now sbp se, Germany, subsequently generated a corresponding 3D finite element discretization for 10-node tetrahedra with 184657 nodes and 114146 elements, see Fig. 23. We thank our colleagues for their kind support.

Similar to Ref. [65], the following load case is defined and investigated. For this, zero boundary conditions are set on surfaces 1 and 7, see Fig. 23, while a load F_2 acts in normal direction on surface 2. The material data for the powder-based alloy AlSi10Mg are chosen for a small strain von Mises plasticity model with the elasticity constants E and ν and the parameters of a linear hardening function $Y(\alpha) = Y_0 + H\,\alpha$ in Eq. (31). Here, α denotes the equivalent plastic strain.

$$\begin{aligned} E &= 70000 \ \ \mathrm{N/mm^2} & Y_0 &= \ \ 230 \ \ \mathrm{N/mm^2} \\ \nu &= \ \ 0.33 \ \ [\text{-}] & H &= 1000 \ \ \mathrm{N/mm^2} \end{aligned} \tag{31}$$

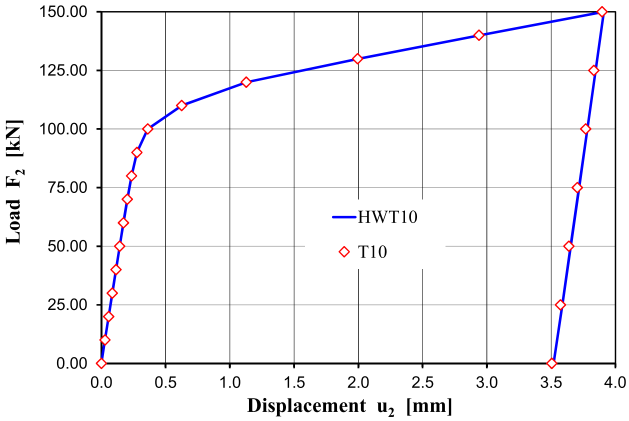

Fig. 24 Load deflection curve F_2 vs. u_2 for a 3D-node

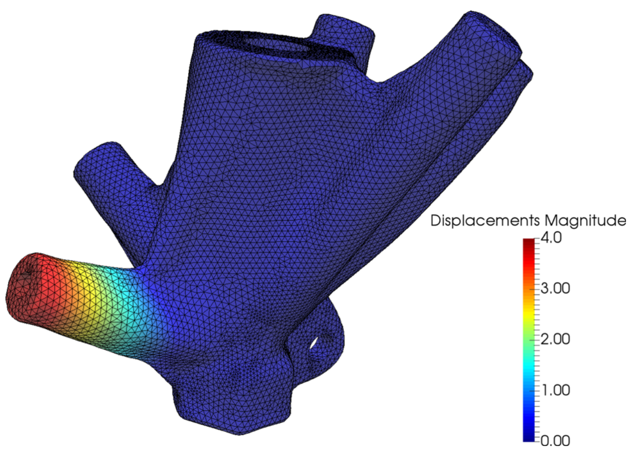

Fig. 25 3D-node with displacements u_m at F_2 = 150 kN

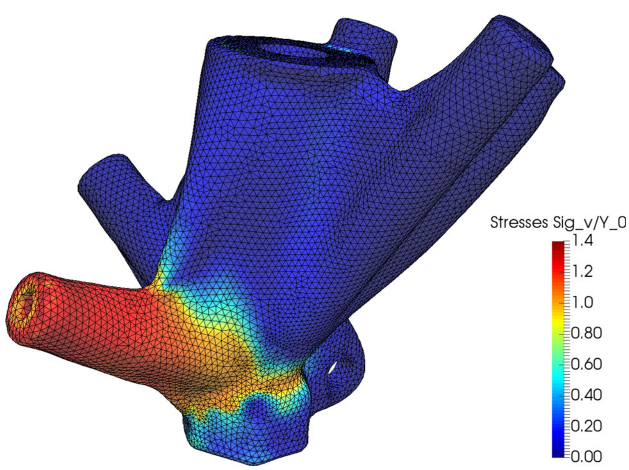

Fig. 26 3D-node with normalized von Mises stresses σ_v/Y_0 at F_2 = 150 kN

Fig. 24 shows the load deflection curves of both elements for the applied normal load F_2 vs. the associated normal displacement u_2.

Since only small displacements occur in the present load case, the robustness advantage of the HWZ10-element does not come into play. With both elements, even the maximum load can be reached in one single load step. However, this can change quickly with a modified system or different loading. Figure 25 depicts the resulting displacements u_m and Fig. 26 shows the normalized von Mises stresses σ_v/Y_0, both at F_2 = 150 kN.

5 Conclusions

A new 10-node mixed-hybrid tetrahedral element based on a Hu-Washizu variational framework is presented. The fulfillment of the 3D patch test is achieved in the common linear version and also in a nonlinear version. The developed element reveals high accuracy for coarse and distorted meshes in static and dynamic problems. The main feature of the element is the remarkable robustness in geometrical and material nonlinear problems. It allows very large load steps and in total less iterations compared to standard displacement elements. This holds especially for thin structures subjected to bending deformations. The element reveals an absolutely stable behavior in the computed examples.

Funding Open Access funding enabled and organized by Projekt DEAL.

References

1. Pian THH, Sumihara K (1984) Rational approach for assumed stress finite elements. Int J Numer Methods Eng 20(9):1685–1695
2. Pian THH, Tong P (1986) Relations between incompatible displacement model and hybrid stress model. Int J Numer Methods Eng 22:173–181
3. Wiśniewski K, Turska E (2008) Improved four-node Hellinger-Reissner elements based on skew coordinates. Int J Numer Methods Eng 76:798–836

4. Viebahn N, Schröder J, Wriggers P (2019) An extension of assumed stress finite elements to a general hyperelastic framework. Adv Model Simul Eng Sci 6:1–22
5. Weissman SL (1996) High-accuracy low-order three-dimensional brick elements. Int J Numer Methods Eng 39:2337–2361
6. Cao YP, Hu N, Lu J, Fukunaga H, Yao ZH (2002) A 3D brick element based on Hu-Washizu variational principle for mesh distortion. Numer Methods Eng 53(11):2529–2548
7. Gruttmann F, Wagner W (2005) A robust nonlinear mixed hybrid quadrilateral shell element. Int J Numer Methods Eng 64:635–666
8. Klinkel S, Gruttmann F, Wagner W (2006) A robust non-linear solid shell element based on a mixed variational formulation. Comput Methods Appl Mech Eng 195:179–201
9. Wiśniewski K, Wagner W, Turska E, Gruttmann F (2010) Four-node Hu-Washizu elements based on skew coordinates and contravariant assumed strains. Comput Struct 88:1278–1284
10. Wiśniewski K, Turska E (2023) Reduced representations of assumed fields for Hu-Washizu solid-shell element. Comput Mech 71:957–990
11. Magisano D, Leonetti L, Garcea G (2017) How to improve efficiency and robustness of the Newton method in geometrically non-linear structural problem discretized via displacement-based finite elements. Comput Methods Appl Mech Eng 313:986–1005
12. Pfefferkorn R, Bieber S, Oesterle B, Bischoff M, Betsch P (2020) Improving efficiency and robustness of enhanced assumed strain elements for nonlinear problems. Int J Numer Methods Eng 122(8):1911–1939
13. Belytschko T, Ong JSJ, Liu WK, Kennedy JM (1984) Hourglass control in linear and nonlinear problems. Comput Methods Appl Mech Eng 43:251–276
14. Belytschko T, Bindeman LP (1993) Assumed strain stabilization of the eight-node hexahedral element. Comput Methods Appl Mech Eng 105:225–260
15. Wilson EL, Taylor RL, Doherty WP, Ghaboussi J (1973) Incompatible displacement models. In: Fenves SJ et al (eds) Numerical and computer models in structural mechanics. Academic Press, New York, pp 43–57
16. Taylor RL, Beresford PJ, Wilson EL (1976) A non-conforming element for stress analysis. Int J Numer Methods Eng 10:1211–1219
17. Simo JC, Rifai MS (1990) A class of mixed assumed strain methods and the method of incompatible modes. Int J Numer Methods Eng 29:1595–1638
18. Simo JC, Armero F (1992) Geometrically non-linear enhanced strain mixed methods and the method of incompatible modes. Int J Numer Methods Eng 33:1413–1449
19. Simo JC, Armero F, Taylor RL (1993) Improved version of assumed enhanced strain tri-linear element for 3D finite deformation problems. Comput Methods Appl Mech Eng 73:53–92
20. Andelfinger U, Ramm E (1993) EAS-elements for two-dimensional three-dimensional plate and shell structures and their equivalence to HR-elements. Int J Numer Methods Eng 36:1311–1337
21. Korelc J, Wriggers P (1996) An efficient 3D enhanced strain element with Taylor expansion of the shape functions. Comput Mech 19(2):30–40
22. De Souza Neto EA, Perić D, Huang GC, Owen DRJ (1995) Remarks on the stability of enhanced strain elements in finite elasticity and elastoplasticity. Communications Numer Methods Eng 11:951–961
23. Wriggers P, Reese S (1996) A note on enhanced strain methods for large deformations. Comput Methods Appl Mech Eng 135:201–209
24. Areias PMA, César de Sá JM, Conceição António CA, Fernandes AA (2003) Analysis of 3D problems using a new enhanced strain hexahedral element. Int J Numer Methods Eng 58(11):1637–1682
25. Reese S, Wriggers P, Reddy BD (2000) A new locking-free brick element technique for large deformation problems in elasticity. Comput Struct 75:291–304
26. Reese S (2005) On a physically stabilized one point finite element formulation for three-dimensional finite elasto-plasticity. Comput Methods Appl Mech Eng 194:4685–4715
27. Reese S (2007) A large deformation solid-shell concept based on reduced integration with hourglass stabilization. Int J Numer Methods Eng 69:1671–1716
28. Korelc J, Šolinc U, Wriggers P (2010) An improved EAS brick element for finite deformation. Comput Mech 46:641–659
29. Pfefferkorn R, Betsch P (2022) Hourglassing- and locking-free mesh distortion insensitive Petrov-Galerkin EAS element for large deformation solid mechanics. Int J Numer Meth Eng 124(6):1307–1343
30. Sauren B, Klarmann S, Kobbelt L, Klinkel S (2023) A mixed polygonal finite element formulation for nearly-incompressible finite elasticity. Comput Methods Appl Mech Eng 403:115656
31. Sauren B, Klinkel S (2024) Mesh topology-based spurious pressure stabilization in 3d finite elasticity using Voronoi tessellations. Comput Mech. https://doi.org/10.1007/s00466-024-02558-1
32. Bonet J, Burton AJ (1998) A simple average nodal pressure tetrahedral element for incompressible and nearly incompressible dynamic explicit applications. Commun Numer Methods Eng 14:437–449
33. Dohrmann CR, Heinstein MW, Jung J, Key SW, Witkowski WR (2000) Node-based uniform strain elements for three-node triangular and four-node tetrahedral meshes. Int J Numer Methods Eng 47:1549–1568
34. Puso MA, Solberg J (2006) A stabilized nodally integrated tetrahedral. Int J Numer Methods Eng 67:841–867
35. Gee MW, Dohrmann CR, Key SW, Wall WA (2009) A uniform nodal strain tetrahedron with isochoric stabilization. Int J Numer Methods Eng 78:429–443
36. Taylor RL (2000) A mixed-enhanced formulation for tetrahedral finite elements. Int J Numer Methods Eng 47:205–225
37. Mahnken R, Caylak I, Laschet G (2008) Two mixed finite element formulations with area bubble functions for tetrahedral elements. Comput Methods Appl Mech Eng 197:1147–1165
38. Mahnken R, Caylak I (2008) Stabilization of bi-linear mixed finite elements for tetrahedra with enhanced interpolation using volume and area bubble functions. Int J Numer Methods Eng 75:377–413
39. Areias P, Matou K (2008) Stabilized four-node tetrahedron with nonlocal pressure for modeling hyperelastic materials. Int J Numer Methods Eng 76:1185–1201
40. de Souza Neto EA, Andrade Pires FM, Owen DRJ (2005) F-bar-based linear triangles and tetrahedra for finite strain analysis of nearly incompressible solids. Part I: formulation and benchmarking. Int J Numer Methods Eng 62:353–383
41. Masud A, Truster TJ (2013) A framework for residual-based stabilization of incompressible finite elasticity: Stabilized formulations and $\bar{F}$ methods for linear triangles and tetrahedra. Comput Methods Appl Mech Eng 267:359–399
42. Gil AJ, Lee CH, Bonet J, Aguirre M (2014) A stabilised Petrov-Galerkin formulation for linear tetrahedral elements in compressible. nearly incompressible and truly incompressible fast dynamics. Comput Methods Appl Mech Eng 276:659–690
43. Lo SH, Ling Ch (2000) Improvement on the 10-node tetrahedral element for three-dimensional problems. Comput Methods Appl Mech Eng 189:961–974
44. Thoutireddy P, Molinari JF, Repetto EA, Ortiz M (2002) Tetrahedral composite finite elements. Int J Numer Methods Eng 53:1337–1351
45. Pakravan A, Krysl P (2016) Mean-strain 10-node tetrahedron with energy-sampling stabilization. Int J Numer Methods Eng 109:1439–1460

46. Pakravan A, Krysl P (2017) Mean-strain 10-node tetrahedron with energy-sampling stabilization for nonlinear deformation. Int J Numer Methods Eng 111:603–623
47. Jabareen M, Hanukah E, Rubin MB (2013) A ten node tetrahedral Cosserat Point Element (CPE) for nonlinear isotropic elastic materials. Comput Mech 52:257–285
48. Kang K, Wen W, Wang P, Duan S, Liang J (2026) A novel 10-node tetrahedral quasi-smooth manifold method and its application in statics analysis of complex geometric structures. Comput Mech 77:729–759
49. Schröder J, Wriggers P, Balzani D (2011) A new mixed finite element based on different approximations of the minors of deformation tensors. Comput Methods Appl Mech Eng 200:3583–3600
50. Bonet J, Gil AJ, Ortigosa R (2015) A computational framework for polyconvex large strain elasticity. Comput Methods Appl Mech Eng 283:1061–1094
51. Taylor RL (2026) FEAP. http://www.ce.berkeley.edu/projects/feap/
52. Keast P (1986) Moderate-degree tetrahedral quadrature formulas. Comput Methods Appl Mech Eng 55:339–348
53. Gellert M, Harbord R (1991) Moderate degree cubature formulas for 3-D tetrahedral finite element approximations. Comm in Appl Num Meth 7:487–495
54. Taylor RL, Simo JC, Zienkiewicz OC, Chan AC (1986) The patch test: a condition for assessing finite element convergence. Int J Numer Methods Eng 22:39–62
55. Schröder J, Wick T, Reese S, Wriggers P, Müller R, Kollmannsberger S, Kästner M, Schwarz A, Igelbüscher M, Viebahn N, Bayat HR, Wulfinghoff S, Mang K, Rank E, Bog T, D'Angella D, Elhaddad M, Hennig P, Düster A, Garhuom W, Hubrich S, Walloth M, Wollner W, Kuhn C, Heister T (2021) A selection of benchmark problems in solid mechanics and applied mathematics. Archives Comput Methods Eng 28:713–751
56. Simo JC (1992) Algorithms for static and dynamic multiplicative plasticity that preserve the classical return mapping schemes of the infinitesimal theory. Comput Methods Appl Mech Eng 99(1):61–112
57. Başar Y, Itskov M (1998) Finite element formulation of the Ogden material model with application to rubber-like shells. Int J Numer Methods Eng 42:1279–1305
58. Başar Y, Ding Y (1992) Finite-rotation shell elements for the analysis of finite-rotation shell problem. Int J Numer Methods Eng 34:165–169
59. Buechter N, Ramm E (1992) Shell theory versus degeneration-A comparison in large rotation finite element analysis. Int J Numer Methods Eng 34:39–59
60. Gruttmann F, Wagner W (2025) A nonlinear 4-node shell element with one point quadrature and stabilization based on a Hu-Washizu variational formulation. Comput Mech 76:613–633
61. MacNeal RH, Harder RL (1985) A proposed standard set of problems to test finite element accuracy. Finite Elem Anal Des 1:3–20
62. Bonet J, Gil AJ, Lee CH, Aguirre M, Ortigosa R (2015) A first order hyperbolic framework for large strain computational solid dynamics. Part I: total Lagrangian isothermal elasticity. Comput Methods Appl Mech Eng 283:689–732
63. Gil AL, Lee CH, Bonet J, Ortigosa R (2016) A first order hyperbolic framework for large strain computational solid dynamics. Part II Total Lagrangian compressible nearly incompressible and truly incompressible elasticity Comput Methods Appl Mech Eng 300:146–181
64. Oberhaidinger F, Gubetini D, Diller J, Bletzinger K-U, Geiser A, Mensinger M (2025) Tensegrity-Turm mit additiv gefertigten Verbindungsknoten f r das Deutsche Museum in M nchen. Stahlbau 94:124–130
65. Ghantasala1 A, Diller J, Geiser A, Wenzler D, Siebert D, Radlbeck Ch, W chner R, Mensinger M, Bletzinger K-U (2021) Node-Based Shape Optimization and Mechanical Test Validation of Complex Metal Components and Support Structures, Manufactured by Laser Powder Bed Fusion, in: Trzcielinski, S. et al. [eds.] Proceedings of the AHFE 2021 Virtual Conferences on Human Aspects of Advanced Manufacturing, Advanced Production Management and Process Control, and Additive Manufacturing, Modeling Systems and 3D Prototyping. AHFE 2021, online, July 25 29, 2021. Cham: Springer Nature Switzerland, pp. 10 17